Conceptual Design and Analysis of Novel Hybrid Auxetic Stents with Superior Expansion

Alireza M.M.Zamani[1], Ehsan Etemadi[2,1,*], Mahdi Bodaghi[3], Hong Hu[2,*]

[1]*Department of Mechanical engineering, Hakim Sabzevari University, Sabzevar, Iran*

[2]*School of Fashion & Textiles, The Hong Kong Polytechnic University, Hong Kong, China*

[3]*Department of Engineering, School of Science and Technology, Nottingham Trent University, Nottingham NG11 8NS, United Kingdom*

Corresponding authors: [*]*hu.hong@polyu.edu.hk, ehsan.etemadi@polyu.edu.hk, etemadi@hsu.ac.ir*

Abstract

This paper presents a conceptual design and finite element (FE) simulation of a novel class of negative Poisson's ratio (NPR) stents with hybrid auxetic structures fabricated by FDM 3D printing technology. The desired structures were first designed in a planar form by a combination of re-entrant, star-shaped, and chiral unit-cells (UCs) but with a difference in the way of connecting UCs to each other. A planar form of the designed stent was 3D printed with thermoplastic polyurethane (TPU) filaments. Then, its mechanical behaviors under quasi-static tensile loading was analysed by the FE method and experimental testing. A good agreement was observed between the FE method and the experiment, and achievement of a significant NPR of -2.3 was revealed. By converting the planar structure into the shape of a stent, the stent expansion and its function were further investigated using the developed FE method based on a complete model consisting of a balloon, plaque, artery, and blood pressure. The results showed that the designed stent has a diameter increase of 96% and 93% at the end of the loading and unloading processes, respectively, which is acceptable according to previous studies. In addition, the distribution of stress in the artery, plaque, and stent and the phenomena of radial and longitudinal recoil, dogboning, and foreshortening of the stent were also investigated. The study revealed that the designed stent could be used as the next generation of polymer stents for vascular diseases in biomedical applications.

Keywords: Auxetic vascular stent, Artery, Finite element analysis, 3D printing, Oden model

1. Introduction

Coronary artery disease (CAD) is the leading cause of death worldwide [1], resulting in the death of approximately seven million people each year [2]. The gradual deposition of fatty substances in the blood, such as cholesterol and triglycerides, leads to the formation of fatty mass called plaque in the inner wall of blood vessels that carry blood to the heart. Plaque causes narrowing or blockage of the arteries, resulting in insufficient oxygen reaching the heart and triggering a heart attack [3].

Medication, bypass surgery, balloon angioplasty, and stent implantation are procedures used to treat clogged arteries. Using stents owing to rapid recovery, less pain, and scar reduction is one of the best treatment methods, and stent implantation has increased in recent years [4]. Stents are small expandable tubes inserted into narrowed arteries to keep the blood supply open. The characteristics of an ideal stent include a superior radial strength to issue, proper arterial support after the final expansion, high radial expanding deformation capability (90% to 100%) to reopen the arteries, small axial and radial recoiling, biocompatibility, small foreshortening, and uniform deformation [5-7]. In addition, comparing the stent models with different geometries and materials allows physicians to use the most efficient model among available stents.

Stent geometry is one of the most important factors affecting the amount of restenosis after stent implantation. The restenosis phenomenon is the diameter reduction of the artery (by more than 50%) after stent implantation, which disrupts the blood flow. This inconvenient phenomenon is directly related to the applied stress on the artery after the stent implantation, which is influenced by the geometry and material of the stent [8]. Stents are often fabricated from metals or polymers. Non-degradable metal stents remain permanently in the artery, which may increase chronic vascular damage and lead to restenosis. Furthermore, these stents suffer from sharp surfaces compared to the arteries [4, 9]. Therefore, polymer stents are suggested instead of metal stents, which can reduce the possibility of thrombosis and restenosis [4, 10].

It is noted that dogboning, foreshortening, and recoil are three considerable problems in the stenting process. Dogboning is the further expansion of the two ends of the stent compared to the central part. Foreshortening is the reduction of the stent length simultaneously as the stent diameter increases. Also, the definition of recoil involves calculating the difference between the mean diameter of the balloon during maximum inflation pressure and the mean diameter of the stent right after the deflation of the balloon [11].

Metamaterials with a negative Poisson's ratio (NPR) are called auxetics [12, 13]. Auxetic structures contract or expand transversely under axial compressive or tensile loading. As a result, they have unique properties such as improved resistance [14, 15], high-energy absorption [16-18], high shear strength [19], and enhanced load-bearing applications [15, 20, 21]. These properties make auxetic materials useful in a wide range of medical [22, 23] and bio-engineering [24-27], including implants [28-30], shields, and medical screws [31-35]. In addition, scientists utilize auxetic tubular structures for various engineering applications [22, 36].

Auxetic materials are found in nature; however, the focus is recently on man-made structures. In auxetic metamaterials, the materials used do not have the NPR values, but the arrangement of the structural struts is in such a way that it exhibits NPR. Re-entrant [37-40], arrow-head

[41-43], star [44, 45], S-shaped [46], and chiral [47] are popular auxetic unit-cells (UCs). The word "chiral" means a molecule that is not superimposable on its mirror image. Meanwhile, anti-chiral structures exhibit reflection symmetry [48, 49]. Chiral structures are named based on the number of struts connected to the central node and developed by the tangential connection of struts to the central nodes [50]. These nodes can be circular, rectangular, or of any other geometric shape. Struts tend to wrap around the nodes under axial loading, and the structure deforms based on the auxetic behavior [51]. Implementing chiral UCs has increased due to the ability to high impact energy absorption [49], light weight, vibration attenuation, and stress concentration [47].

Recently, NPR stents have attracted the attention of biomedical engineers due to their high radial expansion ability and the reduction in damage and risks caused by stent implantation, such as thrombosis and restenosis, compared to conventional stents. An NPR stent has a longitudinal stretch under applied uniform expansion loading by balloon and is placed in the wall of a blood artery. It means that stents with an NPR structure have a high contraction-expansion ratio and can be in contact with a larger surface area of the artery. These structures also avoid common problems in the stenting process, such as stent foreshortening. Additionally, auxetics can improve the mechanical performance of stents and reduce their fracture. This will be useful in the low incidence of restenosis [52].

Li et al. [53] proposed a meta-chiral stent. They examined the mechanical behavior of the designed stent under tensile loading and the effects of geometric parameters on the stent's mechanical properties. They found that the designed stent exhibited NPR property. Wu et al. [54] introduced anti-tetrachiral and hierarchical anti-tetrachiral auxetic stents with circular and elliptical nodes. Their research showed that the foresaid stents could expand significantly in the radial direction while keeping their axial stability.

Hamzehei et al. [55] designed an anti-trichiral stent with circular and triangular nodes. They produced a 2D structure with TPU material by 3D printing and analysed the mechanical behavior of the structure under quasi-static compressive tests. They also fabricated stents on a large scale and investigated their performance via experimental tests and FE analysis. However, they did not consider artery and balloon in conducted simulation. Donik et al. [56] studied the performance of four-layer composite polymer stents. They made sixteen stents with polylactic acid (PLA) and Polycaprolactone (PCL). However, the simulation model for stent expansion did not include plaque and artery. Their work showed that pure PCL stents had less shortening than other stents. Kumar et al. [57] investigated the effect of stent geometrical parameters on radial strength, recoil, foreshortening, and dogboning, without considering the plaque and artery in the FE simulation and compared the results with experimental testing, which showed that the FE model could correctly predict the stent expansion performance. Wu et al. [58] fabricated a biodegradable stent with an auxetic arrow-head structure by 3D printing technology and PLA filament. Their study showed that the shape-memory effect of PLA can benefit for achieving stent expansion under temperature excitation. Lin et al. [4] utilized PLA to print the stent and optimized the structure of the re-entrant UC by conducting a genetic algorithm method. In addition, they studied the mechanical characteristics of the stent by FE and experimental approaches.

Hybrid auxetic structures are developed by combining different UCs to respond the requirement of different applications [59, 60]. Meanwhile, stents with a hybridized UC can

solve the problems above in using the stents. Ruan et al. [61] presented an auxetic stent by combining re-entrant and anti-chiral UCs. In addition, large-scale stents were manufactured by a stereolithography apparatus (SLA) additive manufacturing technique, and their mechanical properties were evaluated through experimental tests and FE simulation. They also investigated the relationship between the geometric parameters and mechanical behavior of the stents by FE simulation and found that the geometry dimensions and arrangement of the nodes affect Young's modulus and Poisson's ratio values of the designed stents.

Although various researchers have proposed different auxetic stents, there is still a need to design stents with a novel hybrid structure which is able to achieve the least required expanding deformation and safe ultimate strength to prevent failure during the stent deployment. Furthermore, a complete model consisting of the artery, plaque, balloon, and blood pressure should be developed to investigate the stent implementation process in a real state.

This study proposed a new hybrid auxetic stent formed with re-entrant, chiral, and star-shaped UCs. First, new types of hybrid auxetic structures were introduced. Then, one planar structure was fabricated using fused deposition modelling (FDM) 3D printing technology for experimental tests. Next, the auxetic behavior of the structure was examined by a quasi-static tensile test, and the results of the experimental tests and FE simulation were compared. Subsequently, the geometrical parameters of the planar structure were analysed. Finally, by rolling the planar structure and converting it to a tubular form, the mechanical behavior of the stent and its expansion performance, such as stress distribution, diameter increase of the stent, recoil, dogboning, and the foreshortening of the stent were investigated using FE method. The simulated models included the stent, artery, plaque, and balloon.

2. Structural design

2.1. Planar meta-chiral structure

This study hybridized re-entrant, star-shaped, and chiral auxetic UCs with high mechanical performance and NPR [43, 57] to develop new auxetic structures. Figure 1 (a-c) shows three designed auxetic structures named S-1, S-2, and S-3 with their UCs (see the red dashed line in Figure 1). These structures were achieved from three different topologies based on how the UCs are connected (see the blue dashed line in Figure 1). In chiral structures, how the struts are connected to the nodes directly affects the structure deformation and strains. Therefore, Poisson's ratio is expected to change with different connections of UCs. The aforesaid planar structures were created by the periodic expansion of their UCs in the *X*- and *Z*-directions.

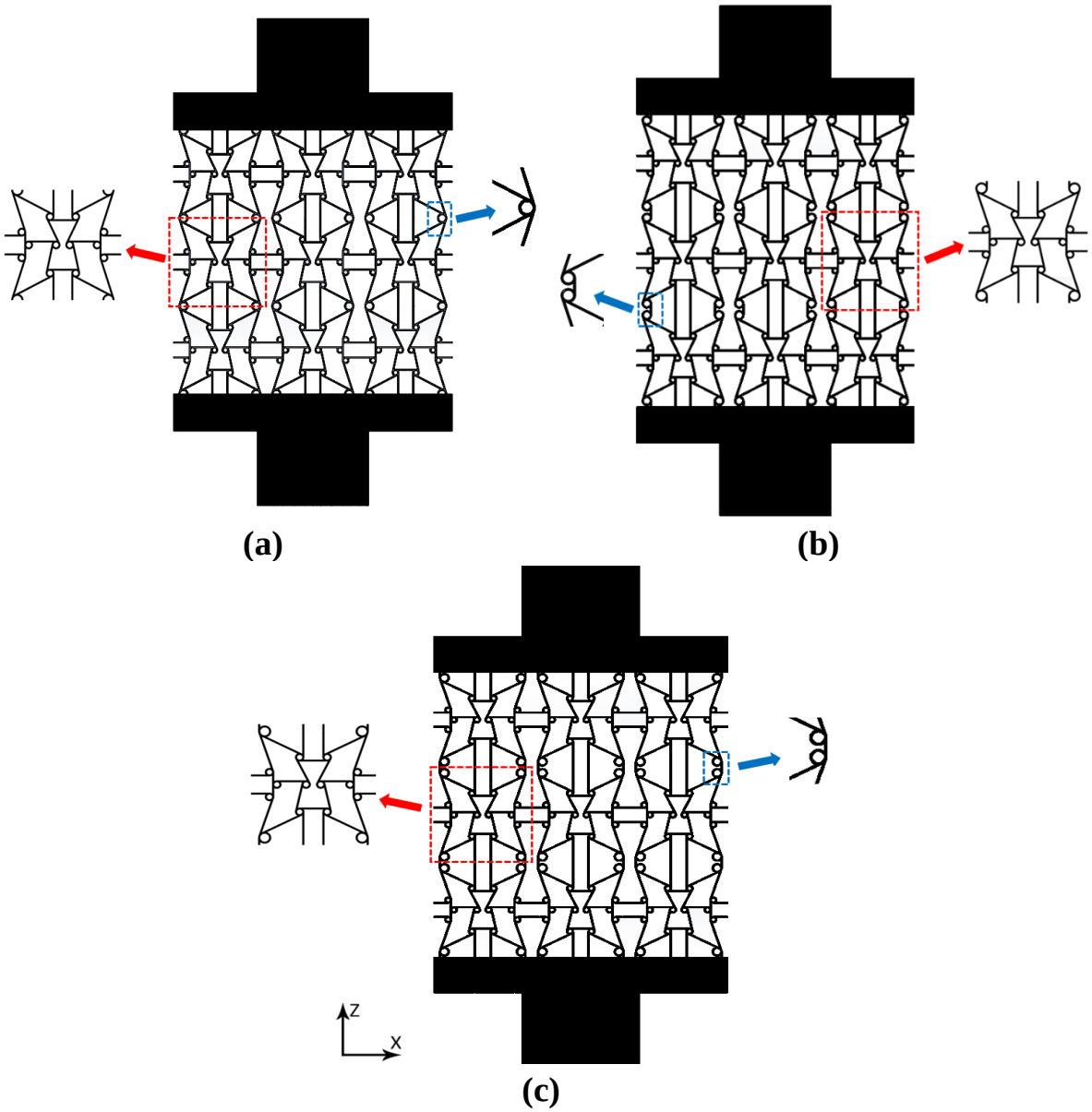

Figure 1. A schematic of the designed structures: (a) S-1 structure, (b) S-2 structure, and (c) S-3 structure.

Figure 2 (a-f) shows the design process of the S-2 UC as an example of the designed hybrid auxetic structures. It was obtained by the combination of re-entrant (Figure 2a), star (Figure 2b), and chiral (Figure 2 (c) and (d)) UCs. The UCs consisted of circular nodes that were tangentially connected by struts. The geometry parameters and dimensions of S-2 UC are shown in Figure 3 and Table 1, respectively. It is noted that the effective parameters for improving the mechanical properties of the stent with S-2 UC were investigated in section 5.2.

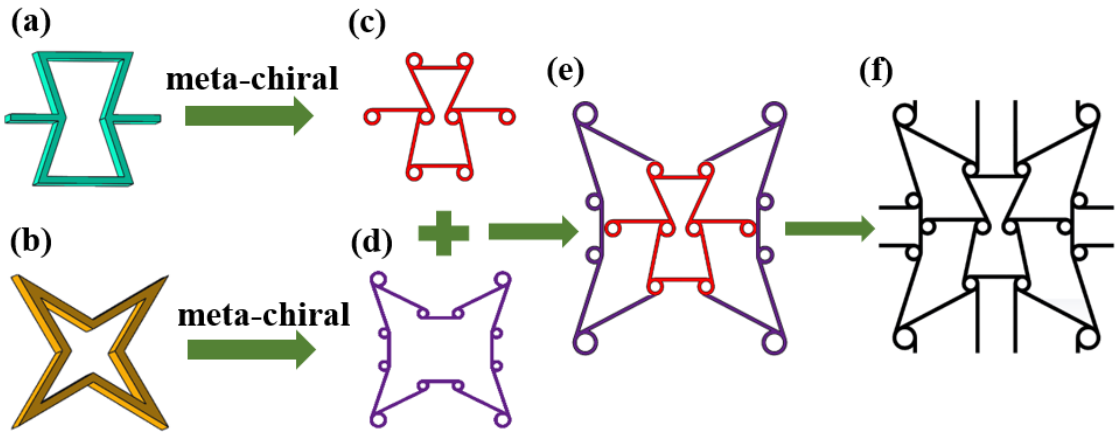

Figure 2. The development process of S-2 UC: a) Re-entrant cell, b) Star-shaped cell, c) Meta-chiral-Re-entrant cell, d) Meta-chiral-Star-shaped cell, e) combination of (c), and (d) f) S-2 UC.

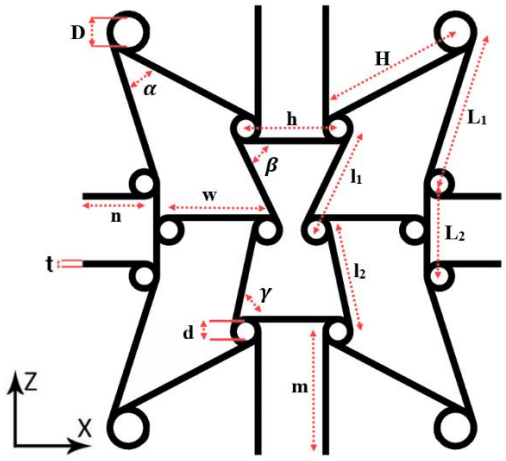

Figure 3. Geometry parameters of S-2 UC.

Table 1. Geometrical parameter values of S-2 UC.

	h (mm)	l_1 (mm)	l_2 (mm)	H (mm)	L_1 (mm)	L_2 (mm)	m (mm)	n (mm)	w (mm)	D (mm)	d (mm)	t (mm)	α (°)	β (°)	γ (°)
UC	11	10.5	12.5	16	16	11	15	7	12	3.7	2.2	0.75	45	64	78

2.2. Auxetic stent structure

The auxetic stent structures were developed by rolling the above designed planar structures into tubular shapes in which UCs are periodically expanded in the radial and axial directions. Figure 4 shows the schematic of the design process for the stent named S-S2 from S-2 UC.

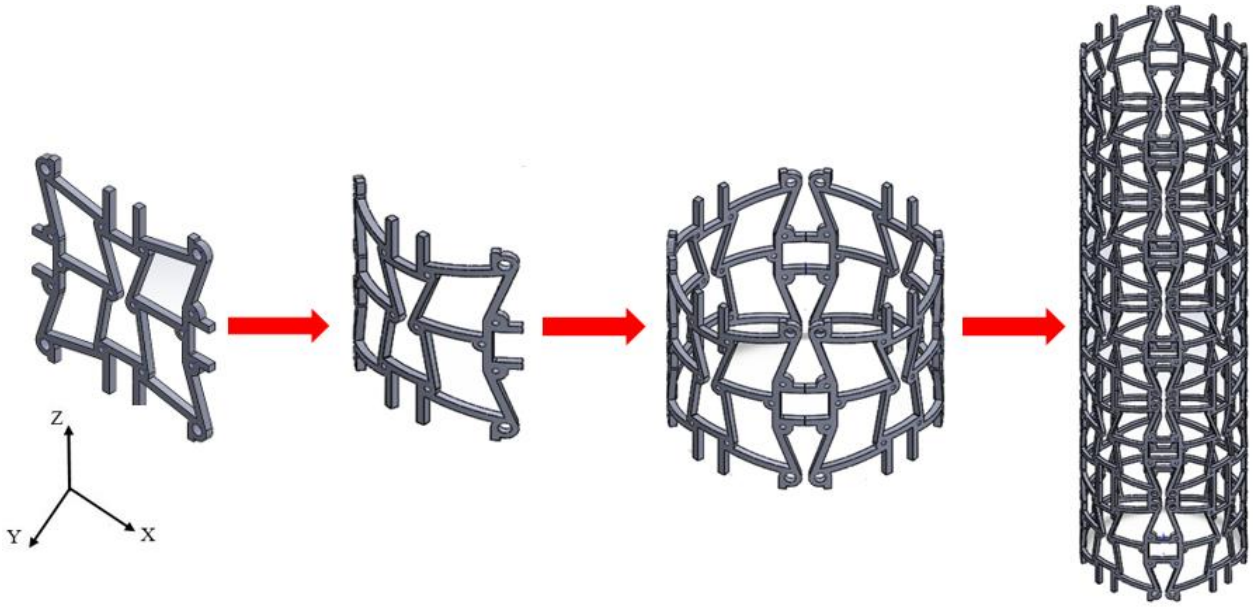

Figure 4. Schematic of the design process of S-S2 stent.

3. Stent implementation simulation (FE simulation of the artery, plaque, stent, and balloon system)

This section presents the simulation of stent implantation in clogged arteries. The simulation of planar auxetic structures was described in Appendix A. 3D FE analysis was developed to simulate the stenting process based on a real scale of constituents, including the stent, artery, plaque, and balloon.

3.1. Artery and plaque simulation

In this study, artery and plaque were considered isotropic and homogeneous. An Ogden hyperelastic model was selected to define their mechanical properties. The values of the Ogden model constants [57] and geometric dimensions are respectively listed in Table 2 and Table 3. In Table 3, L, R_i, and R_o are the length, inner radius, and outer radius, respectively. Two different views of the artery and plaque with geometry parameters are shown in Figure 5. A tie constraint was used to attach the plaque and artery [54].

Table 2. Values of the Ogden model parameters for the homogeneous artery and plaque [62].

Material	$\rho\ (kg/m^3)$	$\mu_1(MPa)$	$\mu_2(MPa)$	$\mu_3(MPa)$	α_1	α_2	α_3	$D_1(MPa^{-1})$
Artery	1070	-4.73	1.70	3.09	-0.39	4.41	-3.25	3.63
Plaque	1450	0.093	-	-	8.170	-	-	0.430

Table 3. Geometric dimensions of the artery, plaque, balloon, and stent.

	L (mm)	R_i (mm)	R_o (mm)
Artery	14	1.9	2.4
plaque	10	0.95	1.9
balloon	12	0.8	0.9
stent	10	1.18	1.25

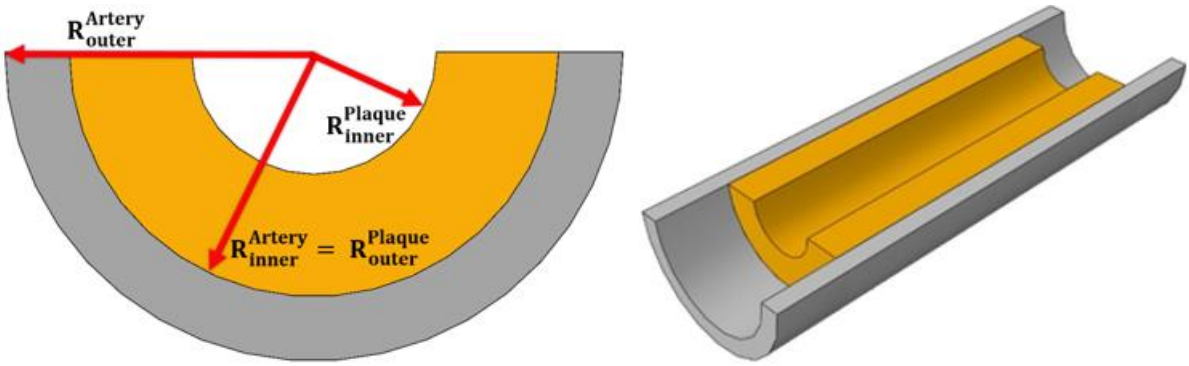

(a) **(b)**

Figure 5. (a) Front and (b) isometric views of artery and plaque.

3.2. Balloon simulation

The stent's diameter was increased by applying uniform pressure using a balloon to expand it. In this study, a polyurethane balloon was used to expand the stent. The hyperelastic Mooney–Rivlin strain energy function was adopted to describe its behavior [62]. The balloon's geometry dimensions and mechanical constants are presented in Table 3 and Table 4, respectively.

Table 4. Values of the Mooney-Rivlin model parameters for the polyurethane [62].

Material	$\rho\ (kg/m^3)$	$C_{10}(MPa)$	$C_{01}(MPa)$	$D_1(Pa^{-1})$
Polyurethane	1070	1.03	3.69	0

3.3. Stent simulation

Geometry dimensions and parameters such as the length and inner and outer diameters of the stent are presented in Table 3 and Figure 6, respectively. A material with high elongation percent was needed so that the stent could reach its desired diameter. To achieve this target, PCL was first selected as a material for the stent with superior flexibility and elongation percent, which had been used to fabricate and simulate stents in previously published works [56, 63, 64]. The elastic-plastic model with linear strain hardening was chosen to describe the mechanical properties of the stent. Table 5 shows the mechanical properties of PCL; however, because of the low melting temperature of PCL and the difficulty in its shipping and transportation, TPU material, which has a high elongation percent similar to PCL, was selected to fabricate the planar structures. While TPU was used to fabricate in-plane structures due to its flexibility and high elongation percentage, its viscoelastic behavior was not suitable for simulating stents, which require a base material with permanent plastic deformation property to prevent the artery from lateral shrinkage. Therefore, PCL was chosen as the base material for the stent simulation. PCL has been shown to exhibit more desirable mechanical properties for stent fabrication, including great elongation and plastic deformation [56, 64].

Table 5. Mechanical properties of PCL [56, 64].

	Density (kg/m^3)	Young's Modulus (MPa)	Poisson's Ratio	Ultimate Strength (MPa)
PCL	1100	300	0.33	30

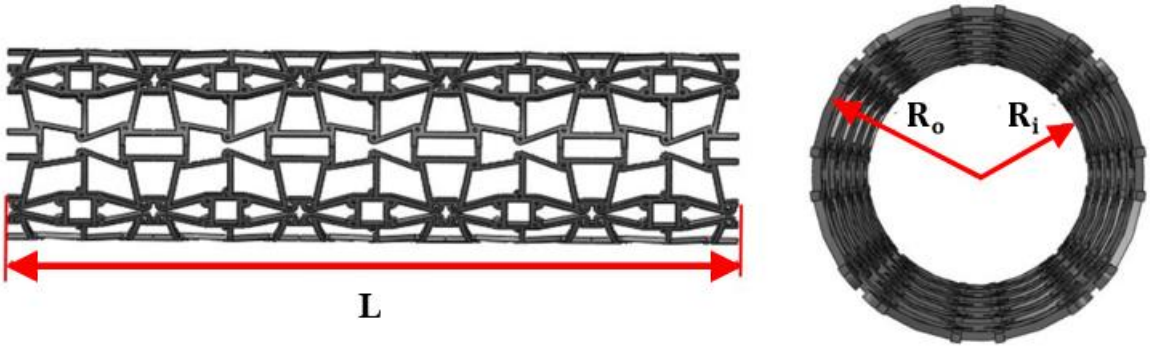

Figure 6. Stent geometric parameters.

3.4. Loading the artery-plaque-stent system

First, the stents were contracted by applying radial displacement in the cylindrical coordinate system, and the diameter decreased. In this state, the stents were compressed from an initial diameter of 2.5 mm to 1.8 mm. It should be noted that the stents were compressed and contracted sufficiently to remain in the elastic region and did not enter the plastic region. Then, the stent expanded by applying uniform pressure loading to the balloon's inner surface, resulting in blood flow due to the opening of the inner surface of the balloon. For this purpose, the interaction properties for the contact between the constituents are surface-to-surface.

Figure 7 shows the artery, plaque, and stent system in the initial state. Only half of the system was simulated due to the model symmetry in the radial direction, and a symmetry boundary condition was applied for the symmetrical surfaces.

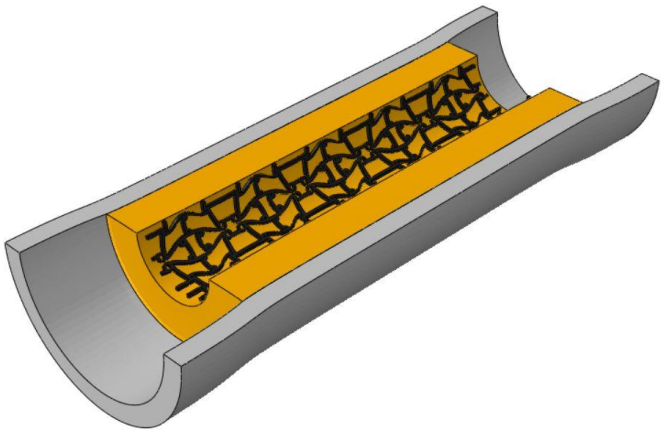

Figure 7. View of the artery, plaque, and stent in an artery system.

The loading process for the models was performed in two steps. In the first step, a pressure equal to the average blood pressure of 100 mmHg was applied to the inner surface of the plaque and the artery. Meanwhile, uniform pressure increasing from zero to 1.17 MPa was also applied to the inner surface of the balloon to expand the stent. In the second step, the pressure applied to the balloon was removed by maintaining the blood pressure applied in the first step, and uniform pressure equal to the blood pressure was applied to the inner surface of the stent.

Figure 8 (a-c) shows the von-Mises stress contour during the loading steps of stent implementation. Figure 8 (a) corresponds to the beginning of the first step, which is the start of loading. In Figure 8 (b), the balloon pressure reaches its maximum, indicating the end of the first step. Finally, Figure 8 (c) shows a view of the balloon-stent-plaque-artery during the unloading step.

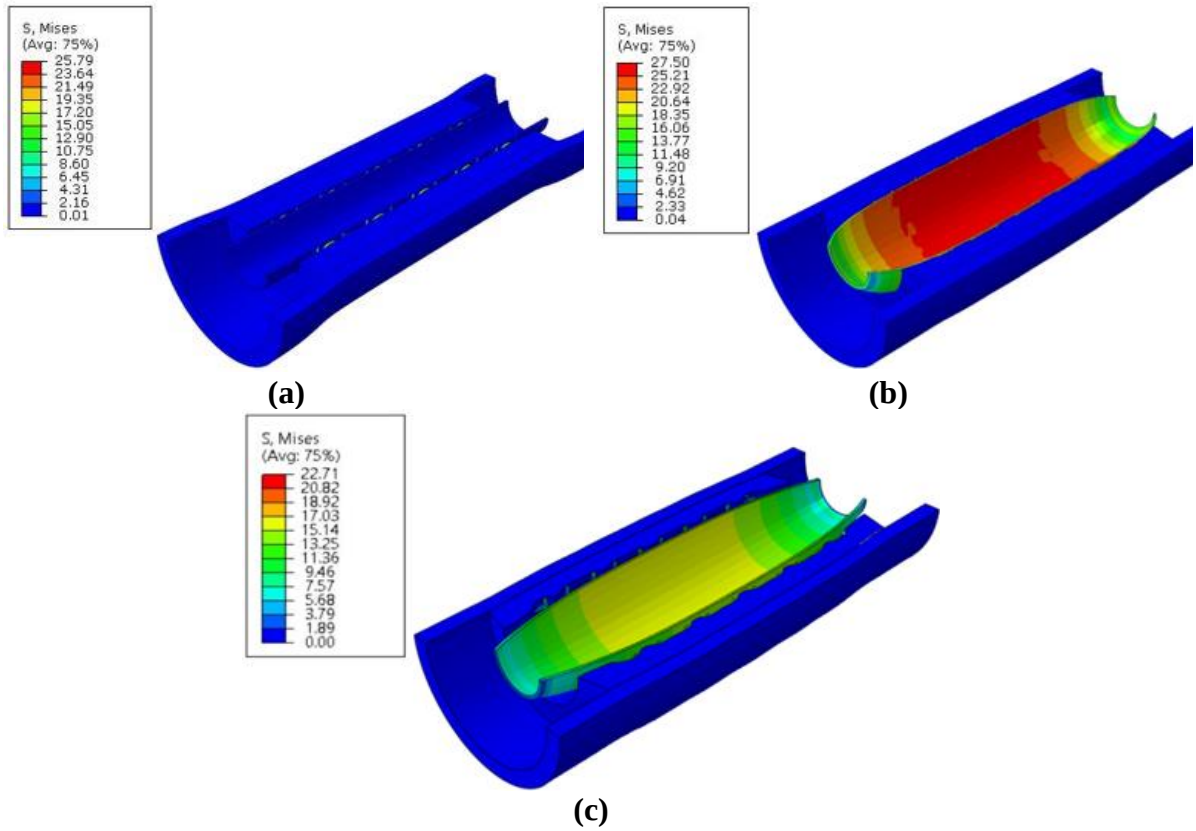

Figure 8. Isometric view of the steps of the FE simulation: (a) the beginning of the loading step, (b) the end of the loading step, and (c) the end of the unloading step.

Similar to planar structures, an 8-node linear 3D block cubic element (C3D8R) was used for the stent, plaque, artery, and balloon meshing. After meshing optimization, the number of elements for each constituent is presented in Table 6.

Table 6. The number of elements used in the FE simulation.

	Artery	Plaque	Stent	Balloon
Number of elements	13400	44000	49500	2900

4. Experimental

4.1. Preparation of samples

This study employed the 3D printing FDM process to fabricate the S-2 structure. Three S-2 structures were manufactured by using a 3D printer Ultimaker with a nozzle diameter of 0.1 mm from the TPU filament. The geometry dimensions of S-2 UC are listed in Table 1. The dimensions of the S-2 samples are 161 mm (length) × 150 mm (width) × 5 mm (height).

4.2. Quasi-static tensile test

The uniaxial quasi-static tensile test was performed on an Instron 5982 testing machine at a temperature of 25 °C and a vertical velocity of 4mm/min to compare the mechanical behaviors of the structures with FE results. During the quasi-static tensile test, the machine directly measured the axial force (F) and longitudinal displacement. The stress can be calculated based on equation (a-2) by measuring the axial force from the load-cell of the machine. Also, the axial strain of the structures in the *Z*-direction was given from equation (a-3).

To measure Poisson's ratio, the lateral and axial displacements of the structures were evaluated with the help of a video camera and Digimizer software. Digimizer is a measurement software of objects in images. Therefore, at the same time as the test, 20 images were recorded with a fixed time interval of 30 s from the deformation of the structure. Pairs of purple and red nodes (similar to Figure A-2 for the FE simulation) were selected to measure the average axial and lateral strains, respectively. Finally, the average Poisson's ratio was measured from equation (a-4).

5. Results and discussion

5.1. Comparison between FE method and experiment

Figure 9 (a) and (b) show the deformation process of the S-2 structure under quasi-static tensile loading for an axial strain interval of 5%, respectively, from the FE simulation and experiment. According to Figure 9, the deformation behaviors of these figures from the FE simulation and experiment are similar, and as a result, this study successfully simulated the behavior of the S-2 planar structure.

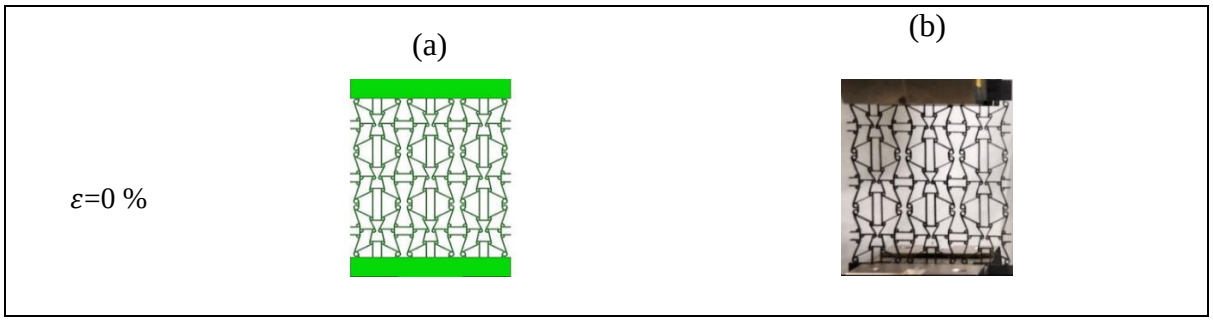

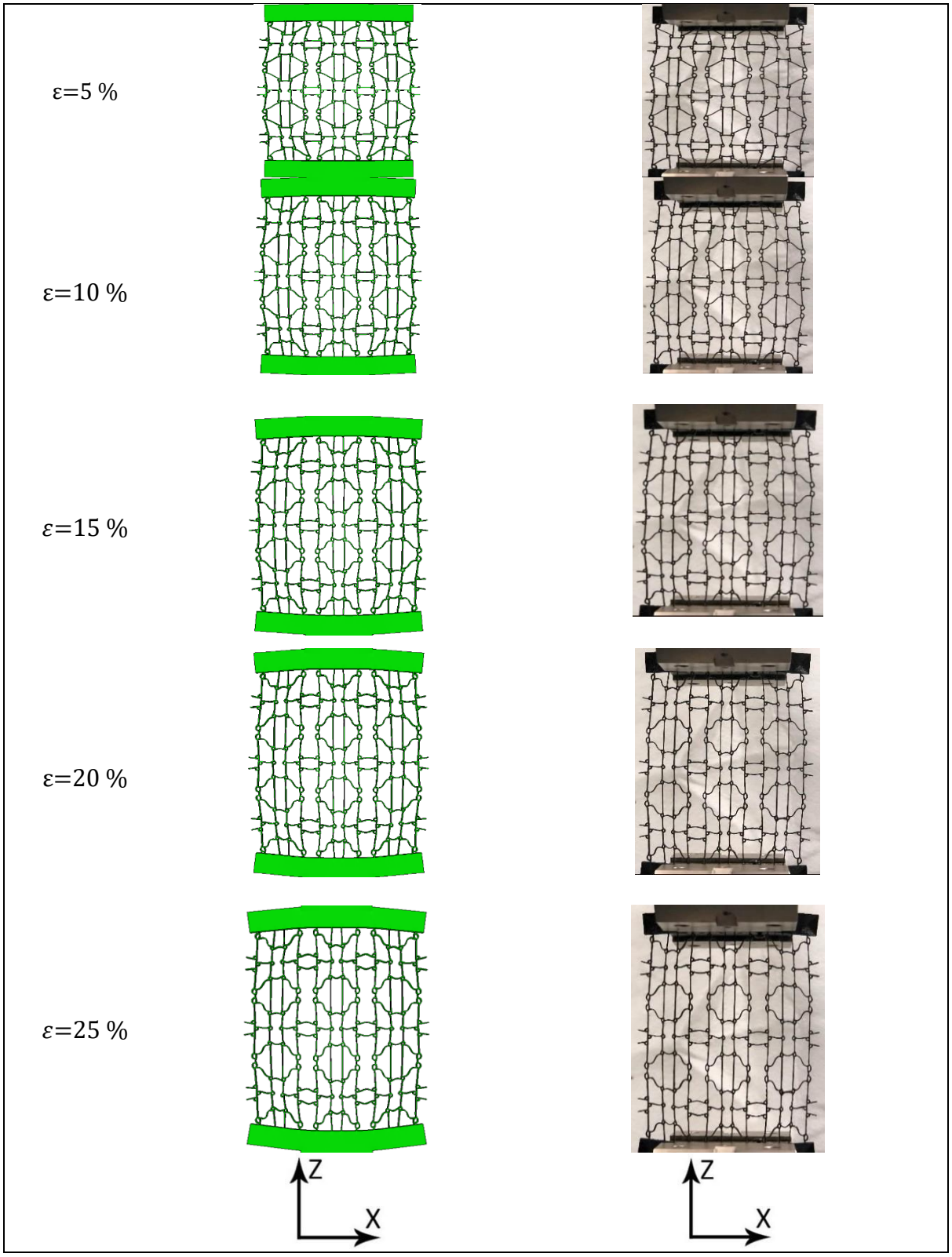

Figure 9. Deformation process of S-2 structure under quasi-static tensile loading at a strain interval of 5%: (a) FE analysis and (b) experimental test.

The stress-strain curves from the tensile experimental test and FE simulation are shown in Figure 10 (a), and the Poisson's ratios as a function of tensile axial strain are shown in Figure 10 (b). Meanwhile, the maximum NPR value obtained from the FE method and the average

values of two experimental tests are listed in Table 7. Figures 9 and 10 and Table 7 show good agreements between the FE simulation and the experimental results. Therefore, it can be derived that the FE method correctly and successfully predicted the behavior of the structure and could be used to investigate other planar designed structures.

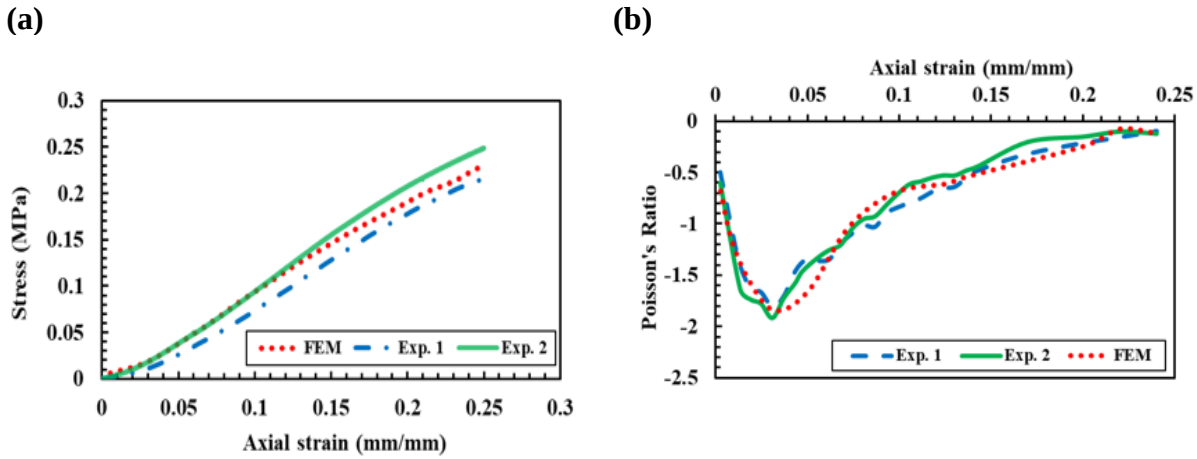

Figure 10. Results of S-2 structure from FE method and experiment: (a) Stress-axial strain curves, (b) Poisson's ratio-axial strain curves.

Table 7. Maximum NPR evaluated from experimental test and FE method.

	FE method	Exp.	Error (%)
Max. NPR	-1.84	-1.80	2.22
		-1.91	3.66

Figure 11 (a) and (b) show the stress-strain and Poisson's ratio-strain curves of the three planar designed structures obtained by the FE analysis, respectively. Focusing on Figure 11 (a) reveals that the stress-strain curves are smooth without fluctuation, in which the stress increases monotonically with increasing strain without an obvious plateau region. There are normally three regions of behavior in the stress-strain curve of a planar auxetic structure: elastic, plateau, and densification regions [46, 65]. However, previous studies [66, 67] have shown that the plateau region is not clearly observed in hybrid re-entrant-chiral structures. Figure 11 (a) confirms this behavior.

Figure 11 (b) shows that these designed structures have the highest NPR at the initial stage of tensile loading as they are extended in both the axial and transverse directions. Under further tensile loading, the tensile force creates a torque on the nodes and causes them to rotate. Therefore, with the rotation of the inclined struts (L_1, l_1, and l_2 as shown in Figure 3) around the nodes and as a result of their placement in the tension direction (Z-direction) (see Figure 12), the deformation behavior of three structures becomes similar. As shown in Figure 11 (b), from the 6% strain, the Poisson's ratio curves of these structures get overlapped, and their NPR effect decreases and tends to zero.

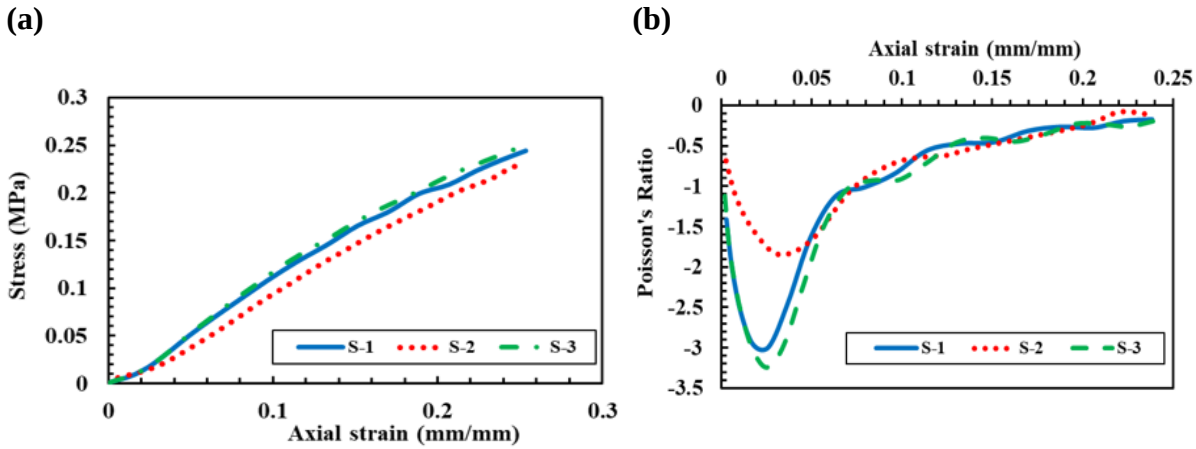

Figure 11. Mechanical behavior of planar designed structures: (a) stress-axial strain curves, and (b) Poisson's ratio-axial strain curves.

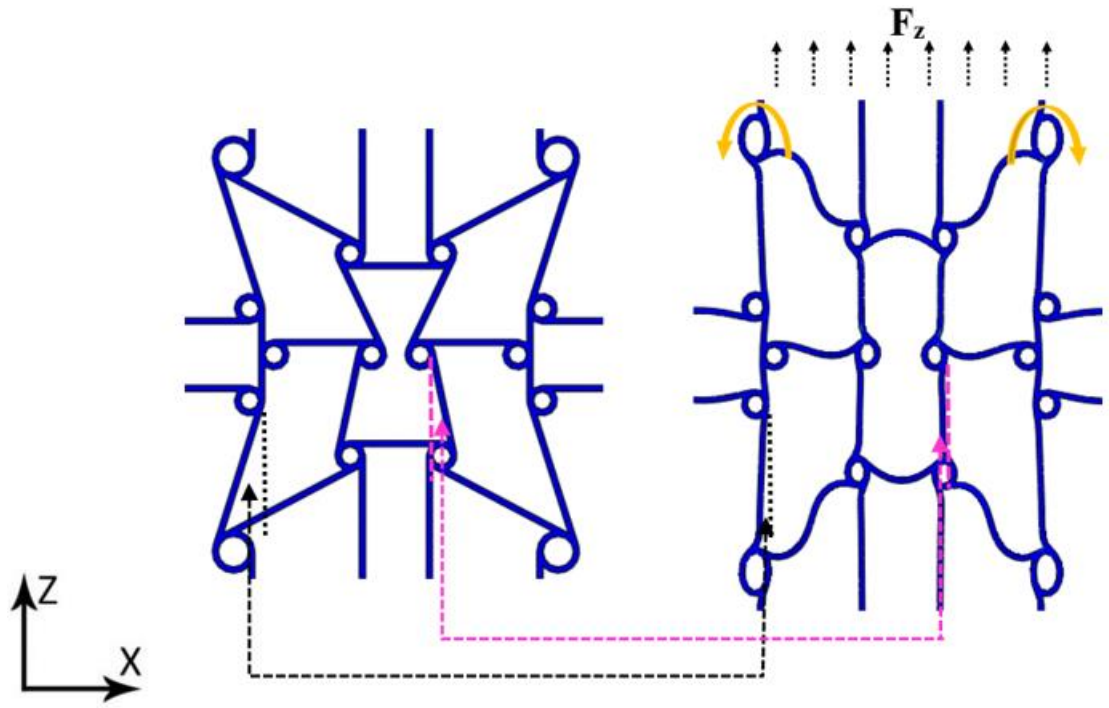

Figure 12. The deformation patterns of a S-2 UC.

Table 8 presents the maximum NPR values of the three planar structures from the FE method. According to Table 8, S-3 and S-2 have the maximum and minimum values of NPR, respectively. In addition, the maximum achieved Poisson's ratio value is -3.2.

Table 8. Comparison of the maximum NPR value of planar structures.

	S-1	S-2	S-3
ν_{max}	-2.98	-1.84	-3.2

5.2. Parametric analysis of the planar structures

It has been demonstrated that the geometrical angles significantly influence the mechanical characteristics of the chiral auxetic structures [61, 66]. Therefore, in this section, the effects of angles α, β, and γ among different geometrical parameters on the Poisson's ratio values of the S-2 structure were evaluated. Two new geometries, named S-2-A-1 and S-2-A-2, were designed, and their angle values are given in Table 9. Other geometry parameters were kept constant, and their values are presented in Table 1. Each structure was subjected to quasi-static tensile loading using the FE method.

Figure 13 shows the variations of Poisson's ratio as a function of axial strain. From Figure 13, the maximum NPR value for each structure is obtained and presented in Table 10. The results show that with an increase in β and γ, which are the angles of the re-entrant part of the UC, the NPR value decreases and tends to zero sooner. In addition, Poisson's ratio decreases with increasing angle α. Therefore, it can be concluded that if the inclined struts of the UC, especially the inclined struts of the re-entrant part (l_1 and l_2), are placed in the direction of tension after applying a greater tensile strain, the NPR increases. By increasing β and γ and then applying tensile strain, the UC nodes were rotated, causing the inclined struts to be rotated to the tensile direction (Z) and become vertical. Subsequently, the UC loses its auxetic property and exhibits a positive Poisson's ratio behavior.

Table 9. Geometrical parameters of UC angles of S-2, S-2-A-1, and S-2-A-2 structures.

structure	α	β	γ
S-2	45	64	78
S-2-A-1	45	70	84
S-2-A-2	50	64	78

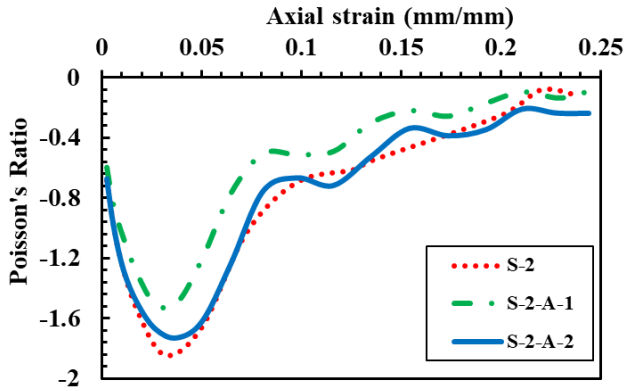

Figure 13. Poisson's ratio curves of three planar structures with different UC angles.

Table 10. Comparison of the highest NPR value of S-2, S-2-A-1, and S-2-A-2.

	S-2	S-2-A-1	S-2-A-2
ν_{max}	-1.84	-1.5	-1.73

5.3. FE simulation of the stent-artery-plaque-balloon system

One of the purposes of this study was to obtain a stent with a diameter increase of 90-100%. However, the diameter increase of S-1, S-2, and S-3 is 82, 96, and 73%, respectively (More details were described in Section 5.3.3). Therefore, because of the greater flexibility of the planar S-2 structure compared to other structures, this structure was selected for the stent, named S-S2. In this section, the FE analysis was conducted to obtain the effective parameters in the S-S2 stent expansion process, including stress distribution on the stent, artery, and plaque, as well as changes in the outer diameter of the stent. In addition, the S-S2 stent's dogboning, recoil, and foreshortening values were presented.

5.3.1. Stress distribution

The stress distribution at the end of the first step (maximum pressure applied to the stent) in the stent-artery-plaque is shown in Figure 14. It should be noted that the image of the balloon was removed owing to a better view of the stress distribution on the stent and plaque, and the stress values shown in the stress distribution figures are in megapascals.

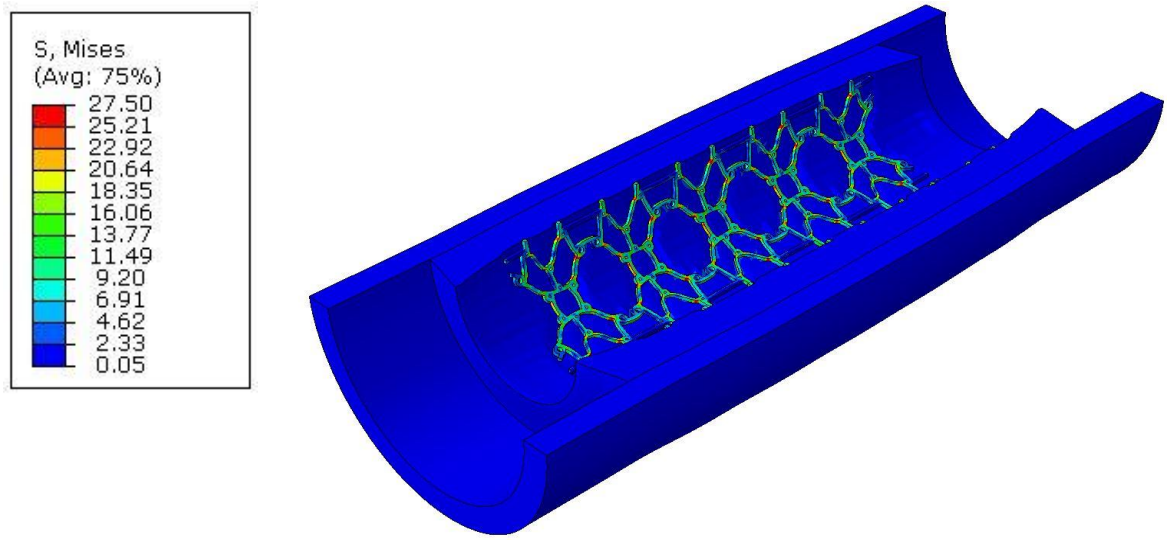

Figure 14. Von-Mises stress distribution on the stent-plaque-artery at the moment of applying the maximum pressure to the stent by the balloon (end of the first step).

Figure 15 shows the stress distribution on the stent at the end of the first step when the maximum balloon pressure (1.17 MPa) has been applied to the stent, in which the balloon, plaque, and artery images were removed. According to Figure 15, the stress distribution in the stent is symmetrical, which is proof of the correct definition of the problem in the FE simulation. From Figure 18, it is also found that the maximum amount of applied stress to the stent is 27.5 MPa. Therefore, considering the ultimate strength value of PCL, which is 30 MPa (see Table 5), the stent has not reached its ultimate strength, and as a result, it does not fail during the loading process.

Figure 15 further reveals that the inclined struts in Figure 3 exhibit the highest stress because they bend with the rotation of the nodes and undergo the greatest deformation. In addition, the struts along the stent, which are blue in Fig. 14(a) (strut m in Figure 3), have the minimum von-Mises stress.

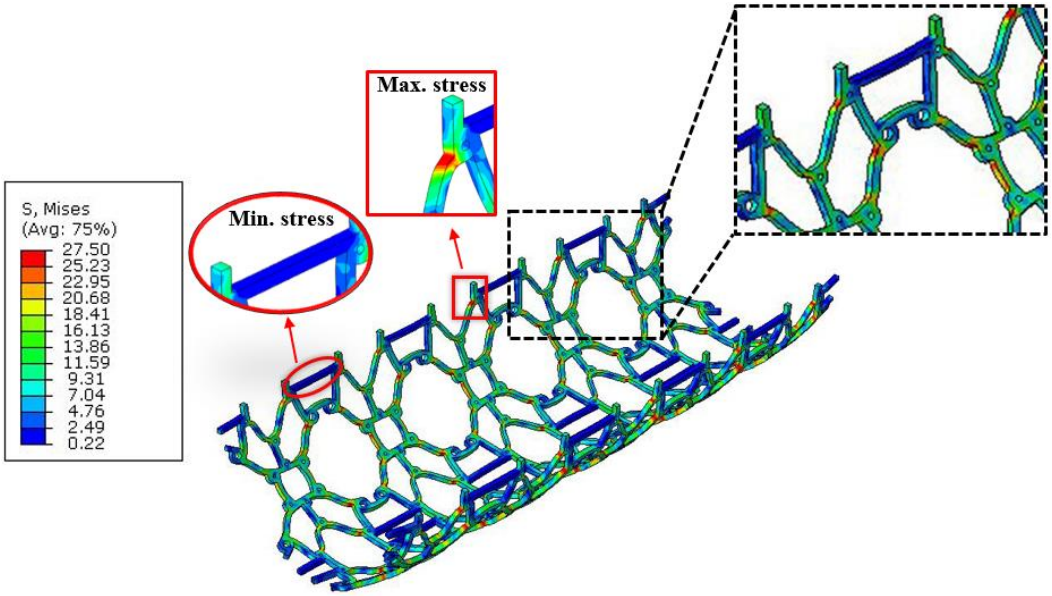

Figure 15. Von-Mises stress distribution on the stent at the moment of applying the maximum pressure (end of the first step).

Figure 15 also shows the stress concentration in the stent (outlined by the black dashed lines). According to Figure 15 and the definition of chiral structures, it can be concluded that owing to the rotation of the nodes and the rotation of the struts around the nodes, the maximum stress occurs at the connection points of the struts to the circular nodes. Therefore, the resistance of the stent against failure can be enhanced by modifying the geometric structure in these areas.

Restenosis after stent implantation is one of the side effects of stents. This phenomenon depends on the applied stress values on the artery and plaque. The risk of restenosis can be reduced by controlling the applied stress to the artery [8]. Figure 16 shows the von-Mises stress distribution in the artery where the balloon, stent, and plaque images are removed for a clearer view. It was found that the maximum von-Mises stress in the artery was 0.225 MPa. According to [64], the maximum applied stresses in the artery due to the expansion of the Palmaz-Schatz, and NIR commercial stents were 0.282 MPa and 0.262 MPa, respectively. Therefore, compared with these two commercial stents, it can be concluded that the proposed stent can reduce the possibility of restenosis in the artery owing to the lower stress applied to it, making it much better than the present generation of fabricated stents.

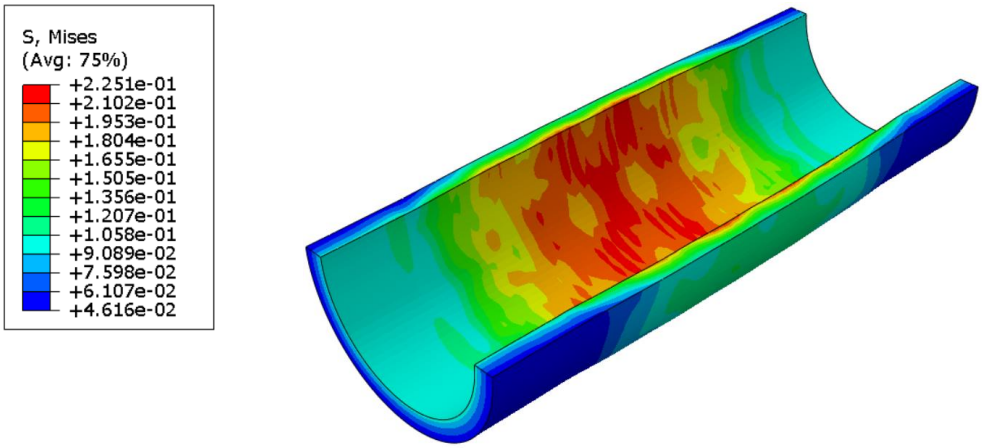

Figure 16. Von-Mises stress distribution in the artery at the end of the loading step.

Figure 17 (a) and (b) show the von-Mises stress distributions in the artery and plaque before and after applying stent pressure to the artery. In this figure, the balloon and stent images were removed for a better view. According to Figure 17 (a), before expanding the stent, a uniform pressure equivalent to the blood pressure (100 mmHg) was applied to the artery and plaque to perform the simulation based on the actual conditions of the stent implementation process. The internal diameter of the plaque after applying blood pressure was 1.9 mm to 2.1 mm. The symmetry in the stress distribution in the plaque, similar to the stent simulation, indicated that the problem simulation was correct. According to Figure 17 (b), the maximum von-Mises stress value for the plaque at the end of the stenting process is 3.29 MPa. It is obvious that the contact point of the stent with the blocking plaque has the highest stress.

In conclusion of this subsection, new stents should be designed to minimize the applied stress value to the artery to reduce the possibility of damage to the artery. Previously published studies [68, 69] have shown that the maximum stress applied to the plaque occurs at both ends of the stent. Due to the bending at both ends of the stent, more stress is applied to the plaque, which can lead to damage to the artery and plaque. In this study, maximum stress did not occur at the end of the stent; rather, the contact point of the stent with the plaque had the highest stress.

(a)

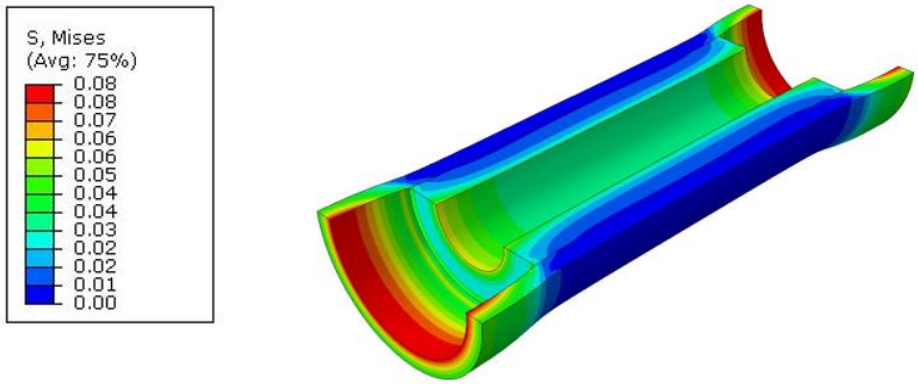

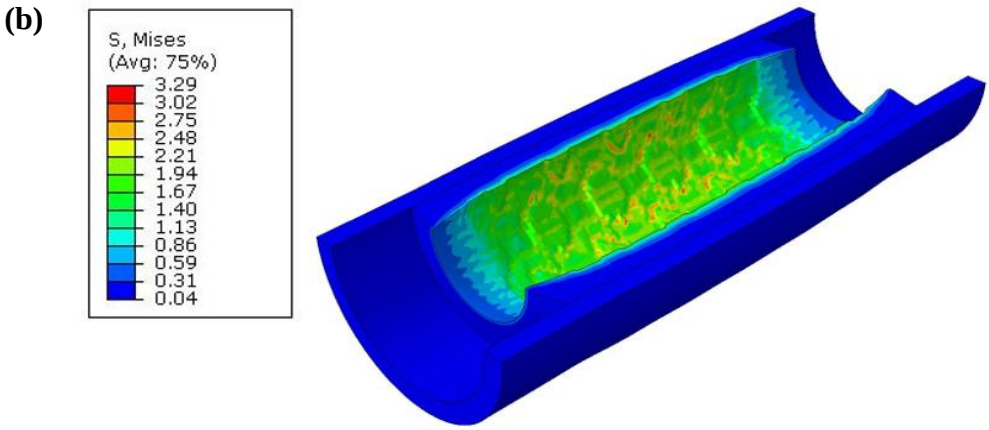

Figure 17. Von-Mises stress distribution in artery and plaque: (a) before applying stent pressure to it and (b) after applying the maximum stent pressure to it.

5.3.2. Checking the equivalent plastic strain (PEEQ) of the stent

Balloon-expandable stents work based on the final plastic deformation of stents. After applying balloon pressure to the stent and increasing its diameter, it maintains its deformed state. Then after removing the balloon and recovering the elastic deformation, the stent should remain in the final plastic deformation state in the artery. Therefore, in FE simulation, it should be checked to ensure that the deformation of the stent is permanent. Figure 18 shows the equivalent plastic strain distribution in the stent at the end of the second step (see section 3.2.5). In this figure, the balloon, plaque, and artery images were also removed for a clearer view. The value of PEEQ must be greater than zero, and according to Figure 18, PEEQ that occurred in the stent is 0.51, which means that the deformation of the stent is permanent and resists the radial pressure of the artery wall and recoil.

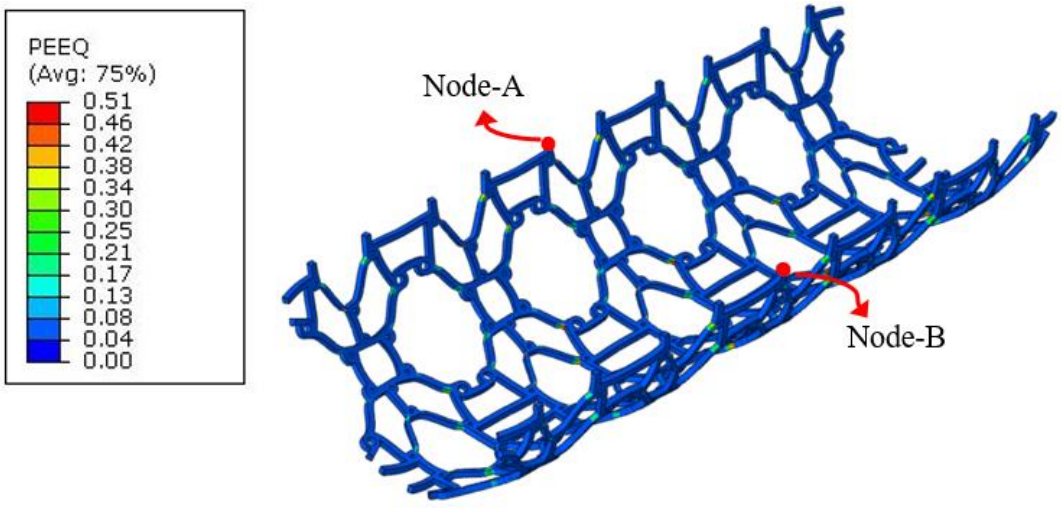

Figure 18. Distribution of the equivalent plastic strain in the stent after the unloading step.

5.3.3. Checking the increase in the diameter of the stent

The trend of stent diameter increase in the FE simulation is one of the most important factors that should be investigated. If the stent is not opened enough, it cannot push the plaque back

and cause the blood supply artery to expand, which practically loses its effectiveness. On the other hand, the artery might be damaged if the stent is overextended. Figure 19 shows the variation curve of the outer diameter of the stent with the pressure applied to it. In this study, the stent's design and material selection was such that it could increase its diameter by 90-100%. The radial displacement values of two pairs of nodes ("Node-A" and "Node-B" in Figure 18) in the middle area of the stent were calculated to detect the increase in stent diameter. According to Figure 19, the stent reached a diameter of 3.53 mm from a diameter of 1.8 mm when the pressure reached its maximum value of 1.17 MPa, corresponding to 96% of the increase in diameter at the end of the loading process. Compared to the previous studies [70], in which the commercial stents of Palmaz-Schatz, NRI, Cipher, and Biomatrix had only 74.25%, 77.15%, 80.78%, and 81.07% of diameter increase, achieving a diameter increase of 96% is a significant achievement of this study.

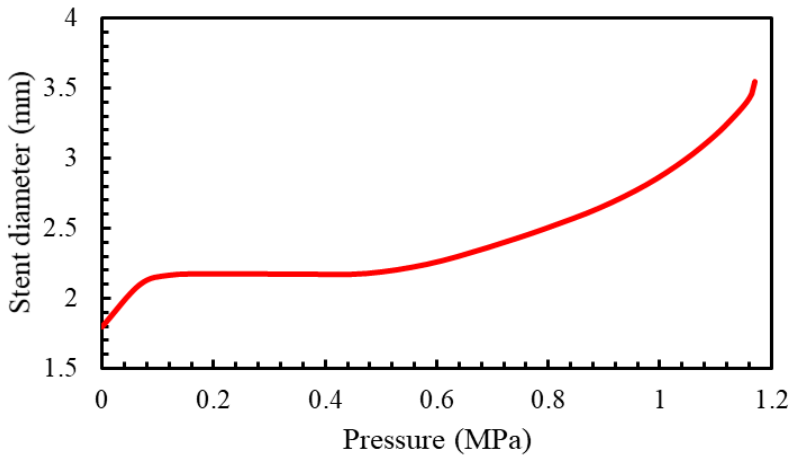

Figure 19. Diameter increase of the stent with applied pressure on it.

5.3.4. Investigation of stent evaluation parameters

Table 11 presents the values of S-S2 stent evaluation parameters such as radial and longitudinal recoil, dogboning, and foreshortening. Dogboning is calculated by the following relation:

$$\text{Dogboning (\%)} = \frac{R_l^d - R_l^c}{R_l^d} \times 100 \quad (5)$$

Where R_l^d is the radius at the end of the stent after applying pressure and R_l^c is the radius at the center of the stent after applying pressure. Recoiling is visible when elastic deformation occurs. After the balloon exits from the artery occlusion site, due to the elastic deformation of the stent and the pressure applied by the artery on the stent, the stent radius and length are reduced, which are called radial recoil and longitudinal recoil, respectively. The following relation describes this phenomenon:

$$\text{radial.recoil (\%)} = \frac{R_l - R_u}{R_l} \times 100 \quad (6)$$

$$\text{longitudinal.recoil (\%)} = \frac{L_l - L_u}{L_l} \times 100 \quad (7)$$

Where R_l and L_l are the radius and length of the stent, respectively, when the maximum pressure is applied, and R_u and L_u are the radius and length after the unloading step, respectively. Foreshortening is calculated by:

$$\text{Foreshortening (\%)} = \frac{L_o - L_l}{L_o} \times 100 \quad (8)$$

L_o is the initial length of the stent and L_l is the length after applying pressure. Foreshortening and dogboning are directly related to damage to the artery. A high radial recoil value also requires more pressure to expand the stent and maintain the required diameter. Higher pressure may damage the plaque and arteries. According to Table 11, the radial recoil after unloading in this study was 43.5% lower than that of the re-entrant-chiral hybrid stent [61]. In addition, the foreshortening and radial recoil for the stent designed in this study were 56.5% and 89% lower, respectively, than those of the composite polymer stent [56].

Table 11. Stent performance evaluation parameters.

	Longitudinal recoil (%)	Radial recoil (%)	Dogboning (%)	Foreshortening (%)
Stent S-S2	0.69	1.13	6.90	10
Ref. [54]	-	10	-	23

According to the values in Table 11, where all parameters are below 10%, it can be concluded that the proposed stent has an excellent quality as it is natural to say that the lower these values and the closer to zero, the better the performance of the stent. Therefore, by analysing the results obtained from the FE simulation of the designed hybrid stent, the low values of foreshortening, recoil, and dogboning, as well as the 96% increase in diameter, show that the desired stent can be introduced as a new generation of stents.

6. Conclusion

In this study, three types of new hybrid auxetic structures were designed, and their behavior under quasi-static tension was investigated. An FDM additive manufacturing method was used to fabricate one of the structures. Then, by performing a quasi-static tensile test, the FE simulation results were compared with the experimental ones, showing good agreement between them. The experimental and numerical studies indicated that the structures initially exhibit the maximum NPR effect when quasi-static tension is applied; however, with the increase of displacement and rotation of all diagonal struts towards the *Z*-direction, the NPR effect decreases, and the Poisson's ratio tends to zero. Therefore, all three structures have the highest NPR at the beginning, which decreases with increasing tension. The highest NPR effect was produced with the S-3 structure at a strain of 2.5%, with a superior value of -3.24.

Among the three designed planar auxetic structures, the most flexible structure was first selected and rolled to develop an auxetic stent. Then, the expansion performance of the

developed stent was further investigated. A complete model of the four parts, including the stent, plaque, artery, and balloon, considering the blood pressure, was proposed to simulate the expansion of the stent inside the narrowed artery. The target artery had 50% local occlusion. By applying balloon pressure, the stent's diameter increases, and, as a result, it applies pressure on the plaque and widens the artery to open the blood flow path. Then, due to plastic deformation in the stent, the pressure of the balloon is removed, and the stent remains inside the artery.

The results showed that the stent has the highest stress at the joint points of the struts and nodes, which leads to the maximum deformations in these areas. This phenomenon could be explained by the fact that struts tangentially connected to nodes in chiral auxetic structures tend to rotate around their nodes during deformation [71]. Meanwhile, the distribution of von-Mises stress in the artery owing to stent expansion was also investigated. Because of lower stress applied to the artery, the designed stent could reduce the possibility of restenosis.

In addition, the maximum increased diameter of the designed stent compared to the initial diameter stent is 96%. The parameters evaluation of the stent further confirmed that the values of radial and longitudinal recoil, foreshortening and dogboning are smaller than 10%, indicating that the high performance of the stent is obtained.

Appendix A. Simulation of planar structures under tensile loading

The Abaqus software package was implemented to simulate the tensile loading test through an FE modelling. The Abaqus is one of the most powerful engineering software applicated in the field of FE analysis that can solve a wide range of industrial issues, from simple to complex problems. Examples include the static and dynamic analysis of metals [72], composites [73], and sandwich structures [74, 75]. On the other hand, SolidWorks software was employed to design the desired planar structures due to the complexity of structural geometries. As a "Step" file format, the designed structures were then imported into the Abaqus software for the subsequent analysis.

In this study, TPU filament was used to print the standard tensile samples and planar S-2 structure. TPU is a biocompatible polymer which has high flexibility, elongation percent, and ductility. Uniaxial tensile tests were conducted according to standard ASTM D638 on an Instron 5982 test machine at a constant velocity of 4 mm/min to obtain the mechanical properties of the material. Three standard tensile printed samples were fabricated and subjected to the tensile tests to obtain trustable results. Their average data are shown in Figure A-1.

A hyperelastic model was used to simulate the mechanical properties of TPU. To evaluate the mechanical constants of a hyperelastic model, the stress-strain data obtained from the uniaxial tensile test of the standard sample were imported to the Abaqus software. From Figure A-1, it can be observed that there is a good correlation between the experimental tensile curve and the Ogden model. Therefore, among available hyperelastic constitutive equations in the Abaqus package, a third-order Ogden hyperelastic model was selected to describe the mechanical properties of TPU. The strain energy potential of the Ogden hyperelastic model was obtained by equation (a-1):

$$W = \sum_{i=1}^{N} \frac{2\mu_i}{\alpha_i^2} \left(\lambda_1^{\alpha_i} + \lambda_2^{\alpha_i} + \lambda_3^{\alpha_i} - 3 \right) + \sum_{i=1}^{N} \frac{1}{D_i} (J-1)^{2i} \quad \text{(a-1)}$$

where λ_i's (i=1-3) are the stretches in three principal directions, μ_i and α_i are material constants, and D_i indicates compressibility. N is the number of terms in the function and can be extended up to N = 6.

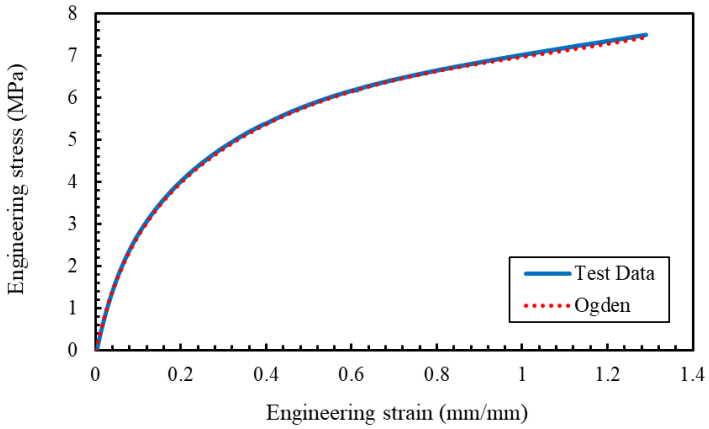

Figure A-1. The comparison between Ogden and the testing data curve.

"All With Self" with tangential behavior was considered to define the interaction between contracted struts. Figure A-2 shows the meshing pattern of the S-2 structure and applied boundary conditions. A displacement-control loading was applied at the top surfaces of the top mandrel in the *Z*-direction. At the same time, the displacement of the bottom surface of the bottom mandrel was fully constrained.

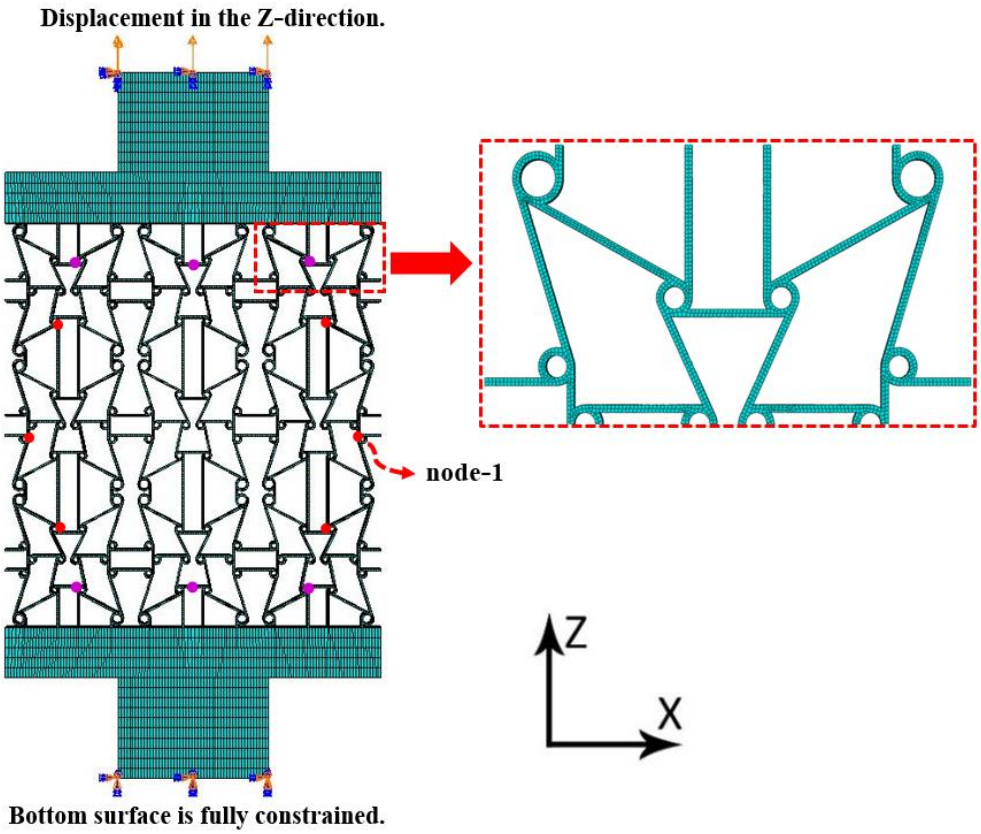

Figure A-2. Boundary conditions and meshing pattern of S-2 structure.

For the meshing of the structures, a three-dimensional cubic element C3D8R with the sweep technique was adopted. In FE analysis, it is necessary to check the mesh sensitivity of the auxetic structure to select the optimized mesh size. Therefore, an element with an 8 mm dimension was first selected for meshing a structure, and the horizontal displacement of a specified node ("node-1" as highlighted in Figure A-2) was evaluated. Subsequently, the element size was reduced to 0.2 mm, and the displacement of the same node was measured. The results indicated no significant change in the displacement of the specified node in the element sizes less than 0.36 mm. Consequently, elements with a dimension of 0.36 mm were selected to mesh the structure.

After calculating the axial force (F) and vertical displacement from the ODB file of the software, the stress and strain of the auxetic structures were calculated using equations (a-2) and (a-3).

$$\sigma = \frac{F}{A} \tag{a-2}$$

$$\varepsilon_z = \frac{\delta_z}{L_z} \tag{a-3}$$

Where A, δ_z and L_z are the cross-sectional area of the structure in contact with the applied load, the displacement value, and the initial length of the structure in the Z-direction, respectively. Therefore, it is possible to plot the stress-strain curve to analyse the mechanical behavior of the structure. To evaluate the Poisson's ratio, as shown in Figure A-2, six pairs of red and purple nodes were selected to measure the average lateral and axial strains, respectively, based on equation (a-3). Then the value of Poisson's ratio was calculated using equation (a-4).

$$\nu_{xz} = -\frac{\varepsilon_x}{\varepsilon_z} \tag{a-4}$$

Where ε_x and ε_z are the transverse and axial strains, respectively.

A dynamic/explicit solver was used to run the tensile tests. In this solver, the internal and kinetic energy values were compared to ensure the accuracy of the quasi-static simulation. To prove that the analysis is based on a quasi-static smooth loading, the kinetic energy should be less than 5% of the internal energy [39]. Figure A-3 shows the kinetic and internal energy histories for the FE simulation of the S-2 structure. According to Figure A-3, the kinetic energy is almost zero, and by comparing the internal and kinetic energies, it can be concluded that the analysis is based on quasi-static loading.

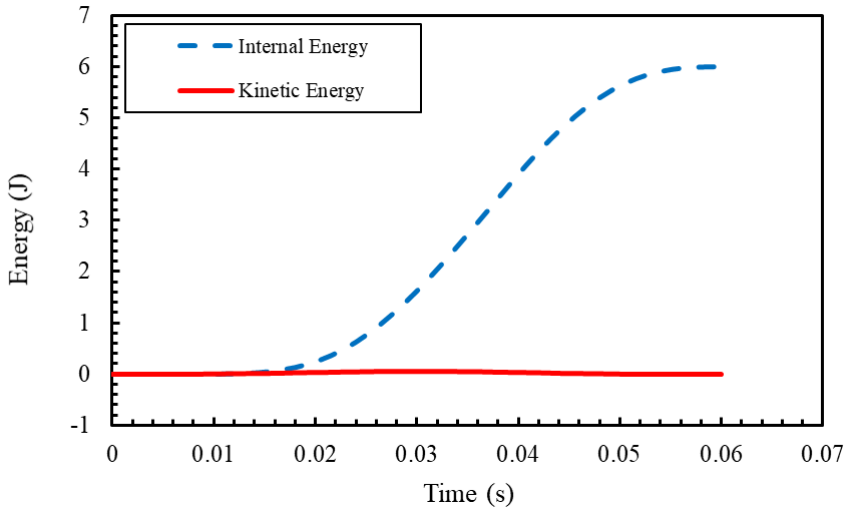

Figure A-3. Comparison of kinetic energy and internal energy of S-2 structure.

References

1. Medina-Leyte, D.J., et al., *Endothelial dysfunction, inflammation and coronary artery disease: potential biomarkers and promising therapeutical approaches.* International Journal of Molecular Sciences, 2021. **22**(8): p. 3850.
2. Ralapanawa, U. and R. Sivakanesan, *Epidemiology and the magnitude of coronary artery disease and acute coronary syndrome: A narrative review.* Journal of Epidemiology and Global Health, 2021. **11**(2): p. 169.
3. He, R., et al., *In silico evaluation of additively manufactured 316L stainless steel stent in a patient-specific coronary artery.* Medical Engineering & Physics, 2022: p. 103909.
4. Lin, C., et al., *4D printing of personalized shape memory polymer vascular stents with negative Poisson's ratio structure: A preliminary study.* Science China Technological Sciences, 2020. **63**(4): p. 578-588.
5. Gori, T., *Restenosis after Coronary Stent Implantation: Cellular Mechanisms and Potential of Endothelial Progenitor Cells (A Short Guide for the Interventional Cardiologist).* Cells, 2022. **11**(13): p. 2094.
6. Zhang, Y., et al., *Model construction and numerical simulation of arterial remodeling after stent implantation with variations of cell concentration.* Medicine in Novel Technology and Devices, 2022. **16**: p. 100144.
7. Zong, J., et al., *Advances in the development of biodegradable coronary stents: A translational perspective.* Materials Today Bio, 2022: p. 100368.
8. Gu, L., et al., *The relation between the arterial stress and restenosis rate after coronary stenting.* Journal of Medical Devices, 2010. **4**(3).
9. Im, S.H., et al., *Current status and future direction of metallic and polymeric materials for advanced vascular stents.* Progress in Materials Science, 2022: p. 100922.
10. Abbaslou, M., R. Hashemi, and E. Etemadi, *Novel hybrid 3D-printed auxetic vascular stent based on re-entrant and meta-trichiral unit cells: Finite element simulation with experimental verifications.* Materials Today Communications, 2023. **35**: p. 105742.
11. Pan, C., Y. Han, and J. Lu, *Structural Design of Vascular Stents: A Review.* Micromachines, 2021. **12**(7): p. 770.

12. Ren, X., et al., *Mechanical properties of foam-filled auxetic circular tubes: Experimental and numerical study.* Thin-Walled Structures, 2022. **170**: p. 108584.
13. Sorrentino, A., et al., *Bio-inspired auxetic mechanical metamaterials evolved from rotating squares unit.* Mechanics of Materials, 2022. **173**: p. 104421.
14. Giménez-Ribes, G., E. van der Linden, and M. Habibi, *Auxetic behavior and unusual shear resistance of crumpled materials: opportunities for programming the nonlinear responses of crumpled mechanical metamaterials.* Materials & Design, 2022: p. 111258.
15. Zhong, R., et al., *Mechanical properties of concrete composites with auxetic single and layered honeycomb structures.* Construction and Building Materials, 2022. **322**: p. 126453.
16. Changfang, Z., et al., *Experimental Study and Finite Element Analysis on Energy Absorption of Carbon Fiber Reinforced Composite Auxetic Structures Filled with Aluminum Foam.* Composite Structures, 2022: p. 116319.
17. Teng, X.C., et al., *A simple 3D re-entrant auxetic metamaterial with enhanced energy absorption.* International Journal of Mechanical Sciences, 2022. **229**: p. 107524.
18. Zhang, W.-M., et al., *A lightweight rotationally arranged auxetic structure with excellent energy absorption performance.* Mechanics of Materials, 2022. **166**: p. 104244.
19. Valle, R., et al., *Evaluation of the Orthotropic Behavior in AN Auxetic Structure Based on a Novel Design Parameter of a Square Cell with Re-Entrant Struts.* Polymers, 2022. **14**(20): p. 4325.
20. Etemadi, E., et al., *Load-bearing Characteristics of 3D Auxetic Structures Made with Carbon Fiber Reinforced Polymer Composite.* Composite Structures, 2023: p. 117206.
21. Etemadi, E., et al., *Improved mechanical characteristics of new auxetic structures based on stretch-dominated-mechanism deformation under compressive and tensile loadings.* Thin-Walled Structures, 2023. **184**: p. 110491.
22. Luo, C., et al., *Design, manufacturing and applications of auxetic tubular structures: A review.* Thin-Walled Structures, 2021. **163**: p. 107682.
23. Shukla, S. and B. Behera, *Auxetic fibrous materials and structures in medical engineering–a review.* The Journal of The Textile Institute, 2022: p. 1-12.
24. Mir, M., et al., *Electromechanically actuated multifunctional wireless auxetic device for wound management.* IEEE journal of translational engineering in health and medicine, 2017. **5**: p. 1-10.
25. Vijayavenkataraman, S., A. Gopinath, and W.F. Lu, *A new design of 3D-printed orthopedic bone plates with auxetic structures to mitigate stress shielding and improve intra-operative bending.* Bio-Design and Manufacturing, 2020. **3**(2): p. 98-108.
26. Jebellat, E., et al., *Numerical investigation of smart auxetic three-dimensional meta-structures based on shape memory polymers via topology optimization.* Journal of Intelligent Material Systems and Structures, 2020. **31**(15): p. 1838-1852.
27. Yarali, E., et al., *Magneto-/electro-responsive polymers toward manufacturing, characterization, and biomedical/soft robotic applications.* Applied Materials Today, 2022. **26**: p. 101306.
28. Chen, D., et al., *Strength enhancement and modulus modulation in auxetic meta-biomaterials produced by selective laser melting.* Acta Biomaterialia, 2022.
29. Jiang, Y., et al., *3D-printed auxetic-structured intervertebral disc implant for potential treatment of lumbar herniated disc.* Bioactive materials, 2023. **20**: p. 528-538.
30. Lvov, V.A., et al., *Auxetic Metamaterials for Biomedical Devices: Current Situation, Main Challenges, and Research Trends.* Materials, 2022. **15**(4): p. 1439.

31. Arjunan, A., et al., *3D printed auxetic nasopharyngeal swabs for COVID-19 sample collection.* journal of the mechanical behavior of biomedical materials, 2021. **114**: p. 104175.
32. Bhullar, S.K., et al., *Characterizing the Mechanical Performance of a Bare-Metal Stent with an Auxetic Cell Geometry.* Applied Sciences, 2022. **12**(2): p. 910.
33. Gao, Y., et al., *New concept of carbon fiber reinforced composite 3D auxetic lattice structures based on stretching-dominated cells.* Mechanics of Materials, 2021. **152**: p. 103661.
34. Kamrul, H., et al., *Geometrical analysis of auxetic woven fabrics based on foldable geometry.* Textile Research Journal, 2022. **92**(3-4): p. 317-329.
35. Kolken, H., et al., *Mechanical performance of auxetic meta-biomaterials.* journal of the mechanical behavior of biomedical materials, 2020. **104**: p. 103658.
36. Scarpa, F., et al., *Mechanical properties of auxetic tubular truss-like structures.* physica status solidi (b), 2008. **245**(3): p. 584-590.
37. Chen, Y. and Z.-W. Wang, *In-plane elasticity of the re-entrant auxetic hexagonal honeycomb with hollow-circle joint.* Aerospace Science and Technology, 2022. **123**: p. 107432.
38. Etemadi, E., A. Molla-Mohammad Zamani, and M. Safikhani-Nasim, *Experimental and numerical analysis of effective geometrical parameters for energy absorbing of the structures with negative Poisson's ratio made from aluminium alloy 1100.* Journal of Solid and Fluid Mechanics, 2021. **11**(1): p. 311-324.
39. Nasim, M.S. and E. Etemadi, *Three dimensional modeling of warp and woof periodic auxetic cellular structure.* International Journal of Mechanical Sciences, 2018. **136**: p. 475-481.
40. Shoja-Senobar, M., E. Etemadi, and M. Lezgy-Nazargah, *An analytical investigation of elastic–plastic behaviors of 3D warp and woof auxetic structures.* International Journal of Mechanics and Materials in Design, 2021. **17**(3): p. 545-561.
41. Francisco, M.B., et al. *Multiobjective design optimization of double arrowhead auxetic model using Lichtenberg algorithm based on metamodelling*. in *Structures*. 2022. Elsevier.
42. Guo, M.-F., H. Yang, and L. Ma, *3D lightweight double arrow-head plate-lattice auxetic structures with enhanced stiffness and energy absorption performance.* Composite Structures, 2022. **290**: p. 115484.
43. Kumar, S., S. Vyavahare, and H. Bogala, *Double Arrowhead Auxetic Structures: A Numerical Investigation Under Compressive Loading*, in *Recent Advances in Manufacturing Modelling and Optimization: Select Proceedings of RAM 2021*. 2022, Springer. p. 35-50.
44. Koutsianitis, P.I., et al., *Conventional and star-shaped auxetic materials for the creation of band gaps.* Archive of Applied Mechanics, 2019. **89**(12): p. 2545-2562.
45. Logakannan, K.P., et al., *Stiffened star-shaped auxetic structure with tri-directional symmetry.* Composite Structures, 2022. **279**: p. 114773.
46. Khadem-Reza, L., et al., *Design of novel 3D auxetic structures based on S-shaped unit-cells.* Smart Materials and Structures, 2022. **31**(7): p. 075024.
47. Wu, W., et al., *Mechanical design and multifunctional applications of chiral mechanical metamaterials: A review.* Materials & design, 2019. **180**: p. 107950.
48. Kelkar, P.U., et al., *Cellular Auxetic Structures for Mechanical Metamaterials: A Review.* Sensors, 2020. **20**(11): p. 3132.
49. Ren, X., et al., *Auxetic metamaterials and structures: a review.* Smart materials and structures, 2018. **27**(2): p. 023001.

50. Zhang, X.G., et al., *A novel auxetic chiral lattice composite: Experimental and numerical study.* Composite Structures, 2022. **282**: p. 115043.
51. Boakye, A., et al., *A review on auxetic textile structures, their mechanism and properties.* Journal of Textile Science & Fashion Technology, 2019. **2**(1): p. 1-10.
52. Carneiro, V. and H. Puga, *Deformation behaviour of self-expanding magnesium stents based on auxetic chiral lattices.* Ciência & Tecnologia dos Materiais, 2016. **28**(1): p. 14-18.
53. Li, H., et al., *In plane mechanical properties of tetrachiral and antitetrachiral hybrid metastructures.* Journal of Applied Mechanics, 2017. **84**(8).
54. Wu, W., et al., *Mechanical properties of anti-tetrachiral auxetic stents.* Composite Structures, 2018. **185**: p. 381-392.
55. Hamzehei, R., et al., *2D triangular anti-trichiral structures and auxetic stents with symmetric shrinkage behavior and high energy absorption.* Mechanics of Materials, 2020. **142**: p. 103291.
56. Donik, Ž., et al., *Computational analysis of mechanical performance for composite polymer biodegradable stents.* Materials, 2021. **14**(20): p. 6016.
57. Kumar, A. and N. Bhatnagar, *Finite element simulation and testing of cobalt-chromium stent: a parametric study on radial strength, recoil, foreshortening, and dogboning.* Computer Methods in Biomechanics and Biomedical Engineering, 2021. **24**(3): p. 245-259.
58. Wu, Z., et al., *Radial compressive property and the proof-of-concept study for realizing self-expansion of 3D printing polylactic acid vascular stents with negative Poisson's ratio structure.* Materials, 2018. **11**(8): p. 1357.
59. Sadegh Ebrahimi, M., R. Hashemi, and E. Etemadi, *In-plane energy absorption characteristics and mechanical properties of 3D printed novel hybrid cellular structures.* Journal of Materials Research and Technology, 2022. **20**: p. 3616-3632.
60. Meena, K. and S. Singamneni, *Novel hybrid auxetic structures for improved in- plane mechanical properties via additive manufacturing.* Mechanics of Materials, 2021. **158**: p. 103890.
61. Ruan, X.L., et al., *Mechanical design of antichiral-reentrant hybrid intravascular stent.* International Journal of Applied Mechanics, 2018. **10**(10): p. 1850105.
62. Schiavone, A. and L. Zhao, *A study of balloon type, system constraint and artery constitutive model used in finite element simulation of stent deployment.* Mechanics of advanced materials and modern processes, 2015. **1**(1): p. 1-15.
63. Guerra, A.J., et al., *3D-Printed PCL/PLA Composite Stents: Towards a New Solution to Cardiovascular Problems.* Materials, 2018. **11**(9): p. 1679.
64. McMahon, S., et al., *Bio-resorbable polymer stents: a review of material progress and prospects.* Progress in Polymer Science, 2018. **83**: p. 79-96.
65. Ingrole, A., A. Hao, and R. Liang, *Design and modeling of auxetic and hybrid honeycomb structures for in-plane property enhancement.* Materials & Design, 2017. **117**: p. 72-83.
66. Alomarah, A., D. Ruan, and S. Masood, *Tensile properties of an auxetic structure with re-entrant and chiral features—a finite element study.* The International Journal of Advanced Manufacturing Technology, 2018. **99**(9): p. 2425-2440.
67. Alomarah, A., et al., *An investigation of in-plane tensile properties of re-entrant chiral auxetic structure.* The International Journal of Advanced Manufacturing Technology, 2018. **96**(5): p. 2013-2029.
68. Cui, F., et al., *EFFECTS OF BALLOON LENGTH AND COMPLIANCE ON VASCULAR STENT EXPANSION.* International Journal of Applied Mechanics, 2012. **02**.

69. Lally, C., F. Dolan, and P. Prendergast, *Cardiovascular stent design and vessel stresses: a finite element analysis.* Journal of biomechanics, 2005. **38**(8): p. 1574-1581.
70. Schiavone, A., L. Zhao, and A. Abdel-Wahab. *Dynamic simulation of stent deployment–effects of design, material and coating*. in *Journal of Physics: Conference Series*. 2013. IOP Publishing.
71. Novak, N., et al., *Development and characterisation of novel three-dimensional axisymmetric chiral auxetic structures.* journal of materials research and technology, 2022. **17**: p. 2701-2713.
72. Zhang, Z., H. Hu, and B. Xu, *An elastic analysis of a honeycomb structure with negative Poisson's ratio.* Smart materials and structures, 2013. **22**(8): p. 084006.
73. Biarjemandi, M., E. Etemadi, and M. Lezgy-Nazargah, *Evaluation of mechanical properties of fiber reinforced composites filled with hollow spheres: A micromechanics approach.* Journal of Composite Materials, 2020: p. 0021998320949649.
74. Imbalzano, G., et al., *Blast resistance of auxetic and honeycomb sandwich panels: Comparisons and parametric designs.* Composite Structures, 2018. **183**: p. 242-261.
75. Toluei, A. and E. Etemadi, *Mechanical properties of multifunctional composite structures with z-pin core using numerical simulation of Hopkinson pressure bar test device.* Journal of Science and Technology of Composites, 2020. **7**(1): p. 683-693.